**Atmospheric
Chemistry
and Physics**

Modeling of 2008 Kasatochi volcanic sulfate direct radiative forcing: assimilation of OMI SO$_2$ plume height data and comparison with MODIS and CALIOP observations

J. Wang[1], S. Park[1], J. Zeng[1], C. Ge[1,6], K. Yang[2,4], S. Carn[3], N. Krotkov[4], and A. H. Omar[5]

[1]Department of Earth and Atmospheric Sciences, University of Nebraska, Lincoln, NE, USA
[2]Department of Atmospheric and Oceanic Science, University of Maryland, College Park, MD, USA
[3]Department of Geological and Mining Engineering and Sciences, Michigan Technological University, Houghton, MI, USA
[4]Atmospheric Chemistry and Dynamics Laboratory, NASA Goddard Space Flight Center, Greenbelt, MD, USA
[5]Science Directorate, NASA Langley Research Center, Hampton, VA, USA
[6]State Key Laboratory of Atmospheric Boundary Layer Physics and Atmospheric Chemistry, Institute of Atmospheric Physics, Chinese Academy of Sciences, Beijing, China

Correspondence to: J. Wang (jwang7@unl.edu)

Abstract. Volcanic SO$_2$ column amount and injection height retrieved from the Ozone Monitoring Instrument (OMI) with the Extended Iterative Spectral Fitting (EISF) technique are used to initialize a global chemistry transport model (GEOS-Chem) to simulate the atmospheric transport and lifecycle of volcanic SO$_2$ and sulfate aerosol from the 2008 Kasatochi eruption, and to subsequently estimate the direct shortwave, top-of-the-atmosphere radiative forcing of the volcanic sulfate aerosol. Analysis shows that the integrated use of OMI SO$_2$ plume height in GEOS-Chem yields: (a) good agreement of the temporal evolution of 3-D volcanic sulfate distributions between model simulations and satellite observations from the Moderate Resolution Imaging Spectroradiometer (MODIS) and Cloud-Aerosol Lidar with Orthogonal Polarisation (CALIOP), and (b) an e-folding time for volcanic SO$_2$ that is consistent with OMI measurements, reflecting SO$_2$ oxidation in the upper troposphere and stratosphere is reliably represented in the model. However, a consistent (∼25 %) low bias is found in the GEOS-Chem simulated SO$_2$ burden, and is likely due to a high (∼20 %) bias of cloud liquid water amount (as compared to the MODIS cloud product) and the resultant stronger SO$_2$ oxidation in the GEOS meteorological data during the first week after eruption when part of SO$_2$ underwent aqueous-phase oxidation in clouds. Radiative transfer calculations show that

the forcing by Kasatochi volcanic sulfate aerosol becomes negligible 6 months after the eruption, but its global average over the first month is −1.3 Wm^{-2}, with the majority of the forcing-influenced region located north of 20° N, and with daily peak values up to −2 Wm^{-2} on days 16–17. Sensitivity experiments show that every 2 km decrease of SO$_2$ injection height in the GEOS-Chem simulations will result in a ∼25 % decrease in volcanic sulfate forcing; similar sensitivity but opposite sign also holds for a 0.03 µm increase of geometric radius of the volcanic aerosol particles. Both sensitivities highlight the need to characterize the SO$_2$ plume height and aerosol particle size from space. While more research efforts are warranted, this study is among the first to assimilate both satellite-based SO$_2$ plume height and amount into a chemical transport model for an improved simulation of volcanic SO$_2$ and sulfate transport.

1 Introduction

Atmospheric sulfate aerosols play an essential role in atmospheric radiative transfer by scattering and absorbing solar and terrestrial radiation (Hansen et al., 1978; Toon, 1982). Although tropospheric sulfate aerosols have a lifetime of a few weeks, their impact on climate change is persistent and

Table 1. Volcanic SO_2 plume modeling studies for the 1991 Pinatubo eruption.

Studies	SO_2 plume heights	Data Sources	Models
Boville et al. (1991)	21–24 km	Ground-based report	3-D CCM2
Tie et al. (1994)	19–26 km	SAGE II	2-D chemical-dynamical-radiative coupled
Bekki and Pyle (1994)	21–28 km	SAGE II	2-D chemical-dynamical-radiative coupled
Zhao et al. (1995)	20–30 km	SAGE II, Lidar	1-D chemical
Timmreck et al. (1999)	19–27 km	SAGE II, Lidar	3-D ECHAM4
Pitari and Mancini (2002)	18–25 km	SAGE II	3-D CCM-CTM coupled
Liu and Penner (2002)	19–26 km	SAGE II, Lidar	3-D DAO GCM
Savarino et al. (2003)	20.5–31 km	SAGE II	2-D chemical-dynamical-radiative coupled
Lohmann et al. (2003)	21.5–29 km	SAGE II	3-D ECHAM4

significant (Seinfeld and Pandis, 2006; IPCC, 2007; Wang et al., 2008). In contrast, stratospheric sulfate aerosols resulting from volcanic eruptions can have lifetimes of 1–3 yr, and hence have more distinct but irregular (or sporadic) effects on global atmospheric chemistry and Earth's radiative energy budget (Budyko, 1977; Hofmann and Solomon, 1989; Deshler et al., 2006). Indeed, oxidation of volcanic SO_2 gas by OH and H_2O_2 is a major pathway for producing stratospheric sulfate aerosols, which are highly scattering and increase planetary albedo in the UV and visible, and this in turn leads to radiative cooling of the Earth's troposphere and surface (Robock, 2000). Through heterogeneous reactions, volcanic sulfate aerosols may also affect chlorine (such as ClO) and nitrogen (such as HNO_3) chemical cycles in the stratosphere, impacting ozone production and destruction mechanisms (Hofmann and Solomon, 1989; Russell et al., 1996; Solomon, 1999). Solomon et al. (2011) showed that stratospheric aerosols have increased in abundance in the last decade, likely due to a series of moderate volcanic eruptions (Vernier et al., 2011), resulting in a radiative forcing of $\sim -0.1\,Wm^{-2}$ in average, counteracting the positive forcing due to anthropogenic CO_2.

Since the Nimbus 7 Total Ozone Mapping Spectrometer (TOMS) detected the SO_2 clouds from the El Chichon eruption in 1982 (Krueger, 1983), satellite measurements have been an indispensable tool for characterizing the spatio-temporal distribution of global volcanic SO_2 emissions. These measurements use the strong SO_2 absorption band at 305–330 nm for retrieval of the total column amount of SO_2. Carn et al. (2003) derived a long-term record of volcanic SO_2 emissions from the TOMS satellites that were in operation nearly continuously from 1978 to 2005. This data record is now being continued and improved with the OMI data (Levelt et al., 2006), and supplemented by solar backscatter ultraviolet (SBUV) measurements from the Global Ozone Monitoring Experiment (GOME) (Burrows et al., 1999) and GOME-2 (Munro et al., 2006), and by infrared (IR) measurements from the Moderate Resolution Imaging Spectroradiometer (MODIS) (Watson et al., 2004), Atmospheric Infrared Sounder (AIRS) (Prata and Bernardo, 2007), Infrared Atmospheric Sounding Interferometer (IASI)

(Karagulian et al., 2010) and Advanced Spaceborne Thermal Emission Spectrometer (ASTER) (Pieri and Abrams, 2010).

However, while satellite-based SO_2 emission inventories provide climate models with a unique description of the spatio-temporal distribution of volcanic SO_2, they provide limited information on the SO_2 vertical distribution. Consequently, current practice is to specify the SO_2 injection height using the volcanic explosivity index (VEI) of the eruption, which is assigned based on many observable parameters available from ground-based reports and is not necessarily an accurate indicator of volcanic SO_2 injection height (Spiro et al., 1992; Simkin and Siebert, 1994; Andres and Kasgnoc, 1998; Robock, 2000). Indeed, in the TOMS SO_2 retrieval algorithm, the SO_2 is assumed to be homogenously distributed below either 5 km or 20 km altitude (Krueger et al., 1995, 2000). Hence, the lack of observation-based characterization of SO_2 plume height has led to various discrepancies in quantification of the climatic effect of volcanic sulfate aerosols. As an example, Table 1 shows a list of different volcanic SO_2 plume heights used in various modeling studies of the 1991 Pinatubo eruption; some studies derived the SO_2 injection height based on the same SAGE (The Stratospheric Aerosol and Gas Experiment) aerosol product, but obtain different estimates. We note that volcanic sulfate aerosols are the result of oxidation of SO_2, and hence, the difference in gravitational settling velocity of SO_2 gas and aerosol particles as well as the vertical variation of atmospheric oxidation capacity can yield discrepancies between the shapes of vertical profiles of volcanic aerosols and SO_2 plumes. Hence, while aerosol vertical profiles can be a good proxy for SO_2 plume injection heights, the direct retrieval of SO_2 plume height from satellite measurements is highly advantageous and is expected to improve modeling of the temporal variation and climatic effects of volcanic aerosols.

In recent years, new-generation satellite instruments such as the polar-orbiting hyperspectral UV sensors (e.g., OMI) and advances in retrieval techniques have expanded our ability to measure volcanic emissions (Clarisse et al., 2008; Eckhardt et al., 2008; Yang et al., 2009, 2010; Rix et al., 2012) beyond the total SO_2 column amount. In particular, Yang et al. (2009, 2010) developed an extended iterative spectral

fitting (EISF) technique to simultaneously retrieve both SO_2 amount and SO_2 altitude from OMI measurements. They found that EISF retrievals of SO_2 plume height were in good agreement with other observations, and their estimate of SO_2 amount has higher accuracy than those derived from the (operational) OMI linear fit retrieval algorithm (Yang et al., 2007).

To demonstrate the value of these advances in remote sensing of SO_2 plumes for climate studies, in this paper we use EISF SO_2 column and altitude retrievals (as in Yang et al., 2009, 2010) to constrain a 3-D global chemical transport model (CTM; GEOS-Chem) simulation of the volcanic aerosol distribution and direct radiative forcing following the August 2008 eruption of Kasatochi (Aleutian Islands). Kravitz et al. (2010) illustrated the importance of 2008 Kasatochi volcanic aerosol forcing on a regional scale, although the climate effect on a global scale appeared insignificant; they assumed a total SO_2 emission of 1.5 Tg which was evenly distributed in three model layers (10–16 km) of a GCM. This study differs from prior modeling studies in that: (a) the CTM is initialized with the direct retrieval of the amount and injection altitude of volcanic SO_2 from OMI, (b) the CTM results are evaluated, and likely causes of uncertainties in the simulation of the volcanic SO_2 lifecycle from transport to sink terms in the atmosphere are diagnosed, with data from multiple A-Train satellite sensors including MODIS aerosol products, MODIS cloud products, additional OMI SO_2 data that are not used to initialize the CTM simulation, and aerosol extinction profiles from the Cloud-Aerosol Lidar with Orthogonal Polarization (CALIOP), (c) a sensitivity study is conducted to analyze the volcanic aerosol forcing as a function of SO_2 injection height specified in the CTM. We describe the satellite data in Sect. 2, the configuration of the GEOS-Chem CTM and the method for calculating volcanic aerosol radiative forcing in Sect. 3, present results of the baseline simulation in Sect. 4 and sensitivity simulations in Sect. 5, and finally summarize the paper in Sect. 6.

2   Satellite data

SO_2 data retrieved from OMI with the EISF algorithm (Yang et al., 2009, 2010) are used in this study to initialize and validate the SO_2 distribution in the model. The EISF technique takes full advantage of the hyper-spectral BUV measurements from OMI to improve the accuracy of SO_2 column retrievals and simultaneously determine the effective altitude of the SO_2 plume. It was designed to address the following two disadvantages of earlier algorithms: (a) a priori assumption of the SO_2 vertical distribution that sometimes results in large errors in the retrieved SO_2 amount; (b) underestimation of SO_2 burdens, especially during large eruptions, because the relationship between BUV radiance and atmospheric SO_2 column increments is assumed to be linear whereas it actually becomes non-linear as the SO_2 burden increases. In the

EISF algorithm, the SO_2 vertical distribution is assumed to be Quasi-Gaussian (with a fixed half width of 2 km in this study), and hence, the EISF retrievals provide an SO_2 amount and effective plume altitude for each OMI footprint (24 km × 13 km at nadir).

The MODIS aerosol optical depth (AOD) product is used to validate our simulation of volcanic sulfate aerosol. The MODIS instruments aboard NASA's Terra and Aqua satellites provide near daily global coverage at their local equatorial overpass times of 10:30 a.m. and 1:30 p.m., respectively (Remer et al., 2005). Since MODIS AOD is a columnar quantity that has limited information about the aerosol chemical composition and aerosol vertical distribution, a direct comparison between MODIS AOD and the modeled volcanic sulfate AOD is not straightforward, in particular when other types of aerosols dominate in the atmospheric column. However, over remote regions where background AOD is generally low, the spatial distribution of high MODIS AOD is still expected to be a good indicator of the transport path or distribution of volcanic aerosol. Hence, we use MODIS AOD for the evaluation of model-simulated transport pathways and distributions (instead of the absolute amount) of volcanic sulfate aerosol. For this purpose, we use the MODIS level 3 AOD product (from both Terra and Aqua) with a spatial resolution of 1° × 1° and an uncertainty of ±0.05 AOD ±0.03 over the ocean and ±0.20 AOD ±0.05 over the land (Remer et al., 2005).

Since in-cloud oxidation is a major sink for volcanic SO_2, the MODIS(MOD08) level 3 cloud product (King et al., 2003) is used to evaluate the accuracy of cloud liquid water and cloud fraction in the GEOS-Chem model, which then provides a basis for the interpretation of any differences between the GEOS-Chem simulated and OMI-observed SO_2 distribution. The cloud information in the MOD08 product is a result of 1° × 1° averaging of MODIS level 2 (MOD06) cloud products that include information on cloud particle phase (water, ice, or mixed), cloud fraction, and cloud optical properties (optical thickness and size for both water droplets and ice crystals). MOD06 is retrieved through a series of algorithms including the cloud mask algorithm at 1 km resolution (Ackerman et al., 1998; Frey et al., 2008) and cloud microphysical retrieval algorithm at 1 km resolution (day-time only) (Platnick and King, 2003). This study uses the cloud fraction and cloud liquid water path (LWP) saved in the MOD08 daily product to compare with counterparts in the Goddard Earth Observing System (GEOS) meteorological fields used by GEOS-Chem. Past analysis showed that the biases in the liquid water path data retrieved from MODIS depend on the cloud type, 3-dimentinoal structure of the clouds (e.g., broken vs. overcast, adiabatic vs. non-adiabatic, etc.), satellite-Sun-Earth geometry, and whether or not having drizzle in the clouds or absorbing aerosols above the clouds (Wilcox et al., 2009; Seethala and Horváth, 2010; Min et al., 2012). In the middle-to-high latitude oceanic region of our interest, Seethala and Horváth (2010) found that

the MODIS liquid water path data overall overestimates the counterpart retrieved from space-borne microwave (AMSR-E) instrument, although significant underestimation can also occur especially for broken clouds. While quantifying the uncertainties in MODIS liquid water path product in our study region and time period is challenging, all past studies support that summation or averaging of MODIS liquid water path over a large spatial domain often reduce the uncertainty (Seethala and Horváth, 2010; Min et al., 2012), which is also the strategy used in this study during the intercomparison of MODIS and GEOS-5 liquid water path (Sect. 4.1).

To evaluate the model simulation of volcanic aerosols in the vertical direction, we compare model results with data from the Cloud-Aerosol Lidar with Orthogonal Polarization (CALIOP) instrument, aboard the Cloud-Aerosol Lidar and Infrared Pathfinder Satellite Observation (CALIPSO) satellite launched in 2006. CALIOP is a two-wavelength (532 and 1064 nm), polarization-sensitive (at 532 nm) lidar that measures atmospheric backscatter with a single-shot vertical and horizontal resolution of 30 m and 333 m, respectively. An extinction-to-backscatter ratio, also referred to as lidar ratio, is needed to convert the aerosol backscatter to extinction. The CALIPSO aerosol algorithm selects a "best-match" lidar ratio after a series of steps. (1) a cloud aerosol discrimination (CAD, Liu et al. 2009) algorithm based upon probability distribution functions (PDFs) of layer averages of 532 nm backscatter, attenuated total color ratio, the midlayer altitude z, and the depolarization ratio is used to separate clouds from aerosols, and to differentiate layers of non-spherical dust particles from layers of spherical particles (e.g., liquid sulfate); (2) based upon the geolocation and season of CALIPSO observations as well as the CAD in step (1), the aerosol type and the lidar ratio are selected from a look-up table that is generated from cluster analysis of AERONET data and in situ observations (Omar et al., 2005; Winker et al., 2009; Winker et al., 2010). To fulfill feature finding and layer classification requirements, the current CALIOP level-2 version 3 algorithm yields an aerosol profile product at a horizontal resolution of 5 km and vertical resolution of 60 m under 20 km altitude. In this study, the quality control flag in the CALIOP level-2 product is used to ensure high quality CALIOP retrievals of aerosol layers for comparing volcanic sulfate aerosols from the GEOS-Chem simulations.

3 Methodology

3.1 GEOS-Chem model, simulation initialization, and sensitivity experiments

A global 3-D CTM, GEOS-Chem (Bey et al., 2001), is used to simulate the evolution of volcanic SO_2. The model is driven by assimilated meteorological data from the GEOS at the NASA Global Modeling and Assimilation Office (GMAO). In this study, version 9-01-01 (http://GEOS-Chem.

org) is used at $2° \times 2.5°$ resolution with GEOS-5 47-level 3-hourly meteorological fields (interpolated at every 15 minutes to match the time step in the GEOS-Chem). Convective transport in the model is calculated from the convective mass fluxes in GEOS-5 meteorological fields (Wu et al., 2007). For boundary layer mixing the non-local scheme is used (Lin and McElroy, 2010). The wet deposition schemes for water-soluble aerosols (Liu et al., 2001) and for gases (Mari et al., 2000) are implemented. Dry deposition is based on the resistance-in-series scheme (Wesely, 1989), with the consideration of the hygroscopic growth of aerosol particles (Park et al., 2004). Anthropogenic emissions of SO_2 in the model use as default the EDGAR 3.2 global inventory for 2000 (Olivier and Berdowski, 2001). The model also uses global biofuel emissions (Yevich and Logan, 2003), anthropogenic emissions for black carbon and organic carbon (Bond et al., 2007), shipping emissions from ICOADS (Lee et al., 2011), biomass burning from the GFED-2 inventory (van der Werf et al., 2009), and a lightning NO_x emissions algorithm (Price and Rind, 1992). Eruptive and non-eruptive volcanic SO_2 emissions for each year are implemented in the model using the AEROCOM hindcast emission data (Fisher et al., 2011), but for the Kasatochi volcanic emissions, we use the OMI EISF data (see description below). The default eruptive volcanic SO_2 data provide daily emissions that are on a generic $1° \times 1°$ grid and are re-gridded into $2° \times 2.5°$ resolution in the model.

Aerosol simulation in GEOS-Chem includes the sulfate-nitrate-ammonium system (Park et al., 2004), carbonaceous aerosols (Park et al., 2003), sea-salt (Alexander et al., 2005), and mineral dust (Fairlie et al., 2007), and couples with gas-phase chemistry (Jacob, 2000) through nitrate and ammonium partitioning (Park et al., 2004), sulfur chemistry (Chin et al., 1996; Alexander et al., 2009), secondary organic aerosol formation (Fu et al., 2008), and uptake of acidic gases by sea salt and dust (Evans and Jacob, 2005; Fairlie et al., 2010). GEOS-Chem includes all major sink terms for SO_2 in the atmosphere, including oxidation by the hydroxyl radical (OH) in the gas phase and by ozone (O_3) and hydrogen peroxide (H_2O_2) in the aqueous phase at temperatures above 258 K (Fisher et al., 2011; Wang et al., 2008a). Stratospheric chemistry in GEOS-Chem is based on climatological representation of species sources and sinks, and uses the Linoz algorithm of McLinden et al. (2000) to simulate stratospheric O_3 (http://wiki.seas.harvard.edu/geos-chem/index.php/Stratospheric_chemistry). The sulfate aerosols are partly or totally neutralized by ammonia (NH_3), and ammonia and nitric acid are partitioned between the gas and the sulfate-nitrate-ammonium aerosol phases using the ISORROPIA II thermodynamic equilibrium model (Fountoukis and Nenes, 2007). A good agreement with no systematic bias was found at the continental scale for comparison of the GEOS-Chem simulated distribution of sulfate-ammonium particles and their extent of neutralization with

those from ground-based observations (Park et al., 2004; Martin et al., 2004).

The current simulation of the evolution of volcanic SO_2 emitted by the Kasatochi eruption was initialized with the spatial distribution of OMI EISF SO_2 amount (Fig. 1a) and effect height (Fig. 1b) on 8 August 2008. SO_2 plumes with column amounts up to 250 DU and effective altitudes up to 10 km can be seen around 52° N, 165° E (Fig. 1a and b). Blocked by a ridge with center line along 155° W (Fig. 1c), the plume was unable to move eastwards, but instead circulated around a low pressure system (centered around 50° N, 170° W) following the anti-clockwise cyclonic flow, and hence quickly diluted westwards, to 50 DU with an effective height of 4–6 km in the downwind region around 50° N, 172° W (Fig. 1a and b). Based upon the distribution of the SO_2 amount and effective altitude respectively in Fig. 1a and b, the vertical distribution of SO_2 (as a function of altitude) is computed under the assumption that its shape follows the Quasi-Gaussian distribution function with a fixed half-width of 2 km (but different effective altitude). This assumption is consistent with that in the EISF algorithm (Yang et al., 2010). The resultant 3-D distribution of SO_2 mass is re-gridded into the GEOS-Chem 3-D grid space to be assimilated into the model (Fig. 1c). In addition, because OMI only provides a snapshot of the distribution of SO_2 during the eruption and also likely missed the western-most part of SO_2 clouds in the study domain of Fig. 1, the estimate of 1.5 Tg of eruptive SO_2 from OMI retrievals may have a low bias (Yang et al., 2010). Consequently, a total of 2.0 Tg SO_2 emission is specified with the effective injection height of 10 km at the model gridbox for Kasatochi. Based upon Waythomas et al. (2010), the eruption duration is assumed to be 24 h (on 8 August 2008) in the model.

It is worthy noting that the assimilation of OMI SO_2 into the model took place in the hour of OMI overpass time, i.e., 23:00 UTC on 8 August 2008, and the assimilation here essentially is the replacement of SO_2 field simulated by GEOS-Chem with the OMI SO_2 field (e.g., similar as model initialization). To avoid the discontinuity of SO_2 field due to this replacement in the model, a Barnes smoothing technique (Barnes, 1964) is used, in which the influence of the innovation (e.g., difference between OMI and molded SO_2) at the model grid box (having OMI SO_2 data) on the change of SO_2 in another gridbox (not having OMI SO_2) is inversely proportional to the distance between these two grid boxes. The purpose of this assimilation is to maximum the use of what OMI observed to correct the model simulation that otherwise would be fully dependent on the specification of the volcanic SO_2 point source function in the model.

Through chemistry inverse modeling constrained by the SO_2 column amount retrieved from AIRS, OMI, and GOME-2, Kristiansen et al. (2010) estimated that the Kasatochi SO_2 emissions may have two peaks at 7 and 12 km above the sea level, and some up to 20 km. This estimate, for the bulk, is consistent with Fig. 1 that shows the peak of SO_2 mixing
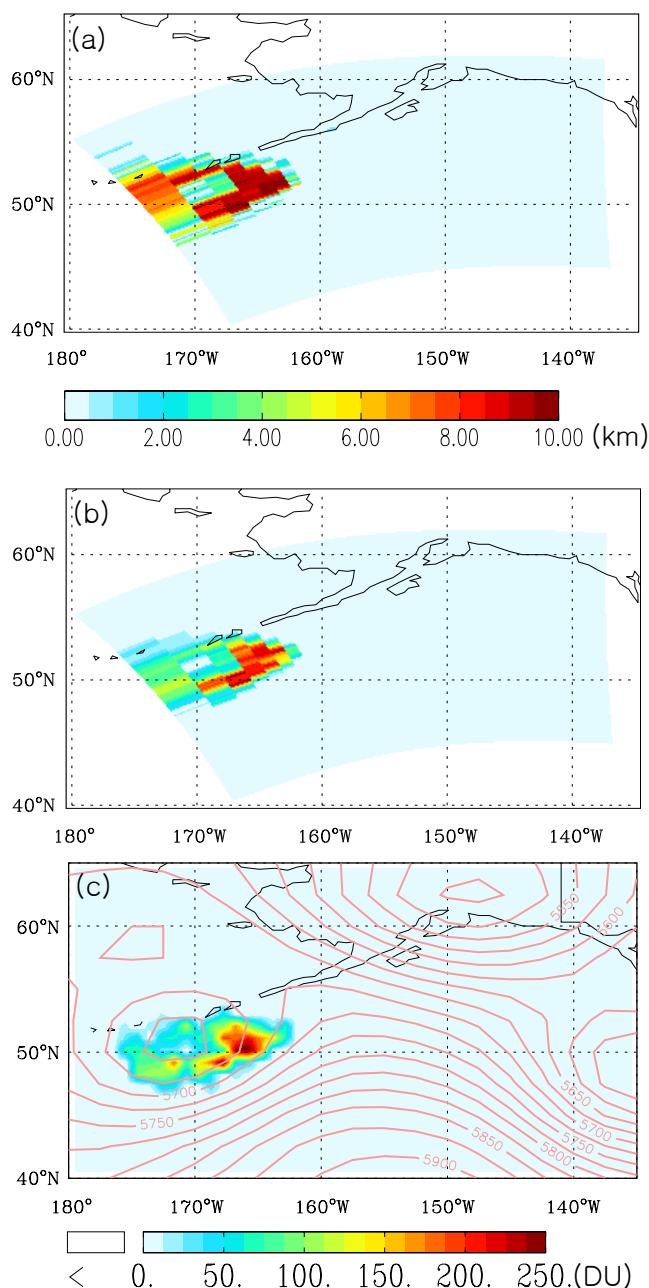

Fig. 1. Kasatochi volcanic SO_2 plume effective height **(a)** and SO_2 column amount **(b)** as retrieved by the OMI EISF algorithm at the OMI footprint resolution on 8 August 2008 (Yang et al., 2009, 2010), and the corresponding SO_2 column amount mapped onto the GEOS-Chem grid box **(c)**. **(c)** is used to initialize the SO_2 distribution in the model. See text for details. The pink solid lines in **(c)** are isopleths (at 25 m intervals) of the 500 hPa geopotential height (in m). For illustration purpose, the SO_2 data in **(c)** is interpolated at 1° × 1° resolution, but is gridded into 2° × 2.5° resolution in the model simulation.
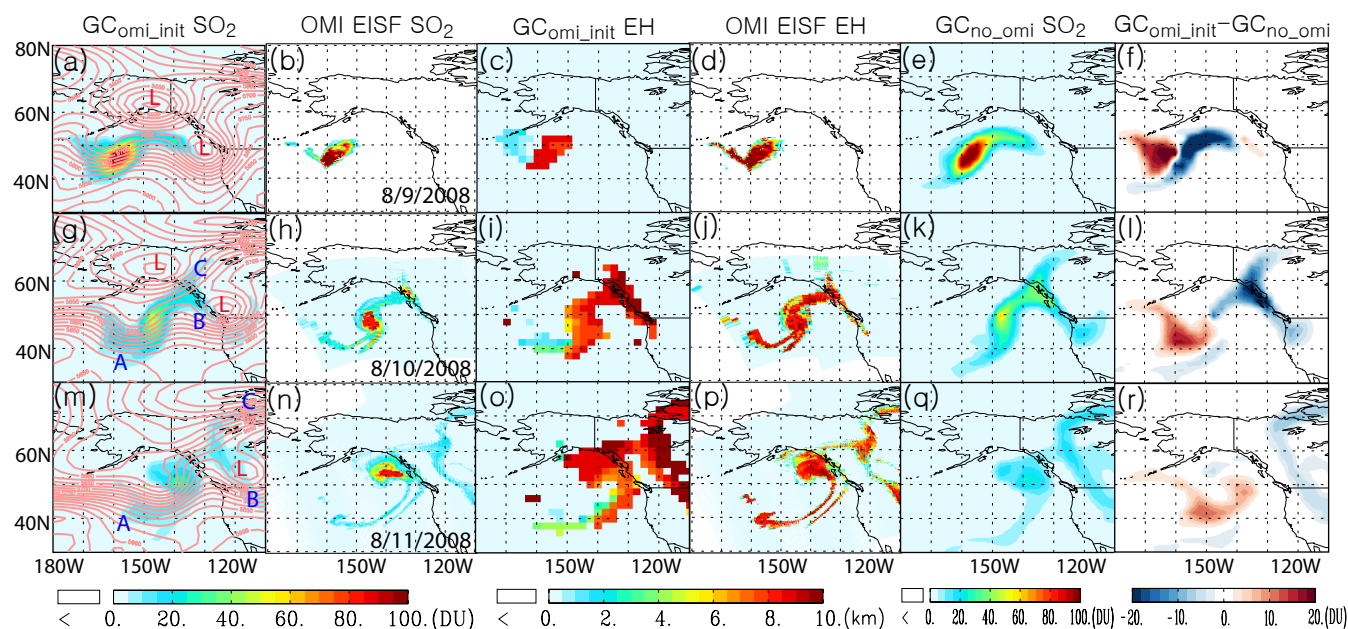
Fig. 2. (a) and **(c)**: distribution of SO_2 column amount (in DU) and effective height (EH) (in km) of SO_2 on 9 August 2008 as simulated by GEOS-Chem (GComi_init) with model initiation of OMI EISF retrieved SO_2 on 8 August 2012; **(b)** and **(d)**: the respective counterparts of **(a)** and **(c)** retrieved from the OMI EISF algorithm; **(e)**: same as **(a)** but from GEOS-Chem simulations without model initiation of EISF retrieved SO_2 (GCno_omi), and **(f)** shows the difference between **(a)** and **(e)**. **(g)**–**(l)** are respectively the same as **(a)**–**(f)** but for 10 August 2008. **(m)**–**(r)** are the same as **(a)**–**(f)** but for 11 August 2008. The pink solid lines in **(a)**, **(g)** and **(m)** are isopleths (at 25 m intervals) of the 500 hPa geopotential height (in m). L in red in **(a)**, **(g)** and **(m)** shows the location of low pressure systems, while A, B, and C in **(g)** and **(m)** respectively mark the three different transport pathways for SO_2. Subscripts omi_init and no_omi respectively denote the simulation with and without initialization of OMI SO_2 data.

ratio is in the range of 6–10 km. However, it also is noted that in model simulation by Kristiansen et al. (2010), the SO_2 emission is specified for two days at the model grid box where Kasatochi is located, and hence their scheme for the initialization of emission is similar to this study, although no OMI SO_2 retrieval are directly assimilated in their model. Nevertheless, both the retrieval of SO_2 amount (such as those from standard OMI product) and retrieval of SO_2 height (such as from research algorithm developed by Yang et al., 2009, 2010) have uncertainties with best estimate of 20 % and 1–2 km respectively; low bias in height retrieval often corresponds to high bias in SO_2 amount retrieval, and vice versa. To investigate the impact of the SO_2 injection height (used after the OMI satellite overpass) on the simulation results, sensitivity simulations are conducted with different injection heights of 2, 4, 6, and 8 km (Sect. 4.2).

3.2 Radiative forcing calculations and sensitivity analysis

Our forcing calculation follows Wang et al. (2008) but with improvement in the treatment of cloud effects. A four-stream broadband radiative transfer model (RTM), employing monthly-mean surface reflectance data (Koelemeijer et al., 2003) and the simulated 3-D aerosol sulfate mass is em-

ployed for the forcing calculations (Fu and Liou, 1993; Wang et al., 2004). The RTM is applied to the solar spectrum for six bands, ranging from 0.2 to 4 μm. The GEOS-Chem simulated volcanic sulfate mass is converted to AOD following Wang et al. (2008) in which the hygroscopic effect on sulfate particle size and refractive index is considered. Band averages of relative-humidity dependent single scattering properties of sulfate aerosols (e.g., single scattering albedo, extinction cross section, and asymmetry parameter) are tabulated in the RTM for computational expediency, while the cloud optical thickness is adopted from the GEOS-5 meteorological field. In the RTM calculations, all aerosol and cloud particles are assumed to be externally mixed (Wang et al., 2008). The difference between upwelling solar irradiances calculated in the presence and absence of sulfate aerosols, without (with) considering the cloud in the RTM calculation, is the clear-sky (all-sky) sulfate direct radiative forcing. In each grid cell, the forcing calculation is conducted every 6 hours because the input cloud properties have 6-hourly temporal resolution.

The optical properties of sulfate particles are based on Wang et al. (2008) in which the size distribution of sulfate particles is assumed to have a lognormal size distribution with geometric dry radius of 0.07 μm and standard deviation of 1.8 μm. While this set of optical parameters is typical for tropospheric sulfate aerosols that often occur in the

neutralized form of ammonium sulfate (Wang et al., 2008), stratospheric volcanic sulfate aerosols may less neutralized (more acid) and thus have greater hygroscopicity than tropospheric sulfate aerosols (Russell et al., 1996). Indeed, within 3–6 months after Pinatubo eruption, the effective radius (or equivalently, geometric mean radius assuming no change in geometric standard deviation) of stratospheric aerosols was shown an increase by a factor of 2–3 (Russell et al., 1996). Wang et al. (2008) estimated that for the same amount of sulfate mass with the same size distribution at RH = 5 %, ammonium sulfate, ammonium bisulfate, and sulfate acid particles can have 20-30 % difference among the radiative forcing efficiencies (normalized to sulfate mass) at RH = 80 %; this difference is primarily due to their different hygroscopic growth. To consider the uncertainty due to hygroscopicity and other factors (such as particle coagulation that are not included in the current GEOS-Chem simulation) in the estimate of particle size, we conducted sensitivity experiments to compute the forcing with different sets of sulfate optical properties with increasing particle geometric radius from 0.07 μm to 0.19 μm (Sect. 3.3).

4 Results

4.1 Baseline results for SO_2 and volcanic sulfate AOD distribution

The model simulation shows that the SO_2 plume, as a whole, moved toward the east after the eruption (Fig. 2a, g and m). The initial SO_2 plume center at 52° N, 165° W on 8 August 2008 dispersed toward the southeast on 9 August 2008 (Fig. 2a) as a result of the southeastward rotation of the major-axis of the low pressure system (originally centered on 52° N, 168° W on Fig. 1c), and on 10 August moved 50° N, 148° W (Fig. 2e). From this center of SO_2 mass on August 10, SO_2 plume extends in several directions (Fig. 2g): (i) toward the southwest (e.g., location A in Fig. 2g) as a result of the blocking ridge along 130° W, (ii) toward the northeast (location C) under the influence of a low-pressure system centered around 65° N, 150° W. However, the flow toward the northeast bifurcates at 55° N, 135° W, with one branch continuing northeast, while another branch moves southeast (location B in Fig. 2g) and then turns northwest in the westerly anti-clockwise flow circulating around another low pressure system centered around 52° N, 125° W. The general SO_2 distribution on 10 August (Fig. 2g) is maintained on 11 August, except that the SO_2 cloud is translated eastward by ~10° latitude with its center at 55° N, 135° W, and SO_2 amounts are more diluted to 20–40 DU on average (Fig. 2m).

Generally good agreement can be found between the modeled SO_2 spatial distribution (Fig. 2a, g and m) and the OMI retrieved SO_2 amount (Fig. 2b, h and n), especially in terms of the location of the volcanic cloud core on 9 August 2008 and the bifurcation of the SO_2 plume on both 11 and 12 Au-

gust 2008. However, the modeled patterns overall are more diffuse than the OMI observations (Fig. 2), likely reflecting the difference between the GEOS-Chem model grid size (2° × 2.5°) and the OMI footprint size (24 km × 13 km at nadir) and the non-ideality in the model (as discussed below). In addition, the inability of OMI to retrieve SO_2 located beneath clouds also can partially explain why the flow of SO_2 is not as continuous and smooth as that in the model simulations.

In addition to the overall agreement between modeled and OMI retrieved spatial distribution of SO_2 amount, the GEOS-Chem modeled distribution of SO_2 effective height on 9–11 August 2008 (Fig. 2c, i, and o) is also consistent with the counterparts of OMI EISF retrievals (Fig. 2d, j, and p). Both model and OMI retrievals show that the core of SO_2 plume was generally maintained at the effective height of 10 km, but the effective height for the part of SO_2 plume in the southwest direction (C in Fig. 2g and C in top-right corner of Fig. 2m) decent to about 2–4 km. In the comparison, it is noted that OMI is not sensitive to SO_2 plumes at low altitude.

Contrast between GEOS-Chem simulations with and without initialization of using OMI EISF SO_2 data shows significant differences (up to ± 20 DU) in the spatial pattern of SO_2 distribution (Fig. 2f, l, and r) during 9–11 August 2008. However, in comparison to the OMI retrievals, it is clear that the simulation with the assimilation of OMI EISF SO_2 data gives a better description of the SO_2 transport. The simulation without assimilation of OMI EISF SO_2 appears to give a faster dilution of SO_2 from the core, and therefore, an overestimation of SO_2 in locations such as A, B, and C marked on Fig. 2g and 2m (Fig. 2f, l, and r). In addition, in the southwest direction (along location A), the simulated SO_2 without assimilation reaches too far to the south (around 30° N) on 10–11 August 2008, while both OMI and simulation with assimilation show the SO_2 plume only reaches around 38° N. Quantitatively, the simulated SO_2 with assimilation have a correlation coefficient of 0.73 and normalized root-mean square difference of (with respect to OMI retrievals) 1.25, while without assimilation respectively have 0.63 and 1.53, with OMI SO_2 (after re-gridding to GEOS-Chem grid). Such improvement through assimilation may be useful to short-term prediction of the movement of volcanic SO_2, which can have important implications for aviation weather forecast.

Quantitative comparisons with OMI SO_2 data show that GEOS-Chem underestimates SO_2 columns by over 20 DU in the plume core on August 10, and by ~60 DU on August 11 (Fig. 2). Further comparison of the 40-day time series of modeled and EISF-retrieved total SO_2 burden after the eruption shows that the model underestimation appears persistent throughout the simulation (Fig. 3). Figure 3a also shows that the modeled evolution of total SO_4^{2-} mass is consistent with the temporal evolution of total SO_2 mass, and is peaked around the end of August and early September. Heard et al. (2012) showed that with the use of their profile 1 of SO_2 emission (i.e., 10 % in 5.5–6.5 km, 50 %
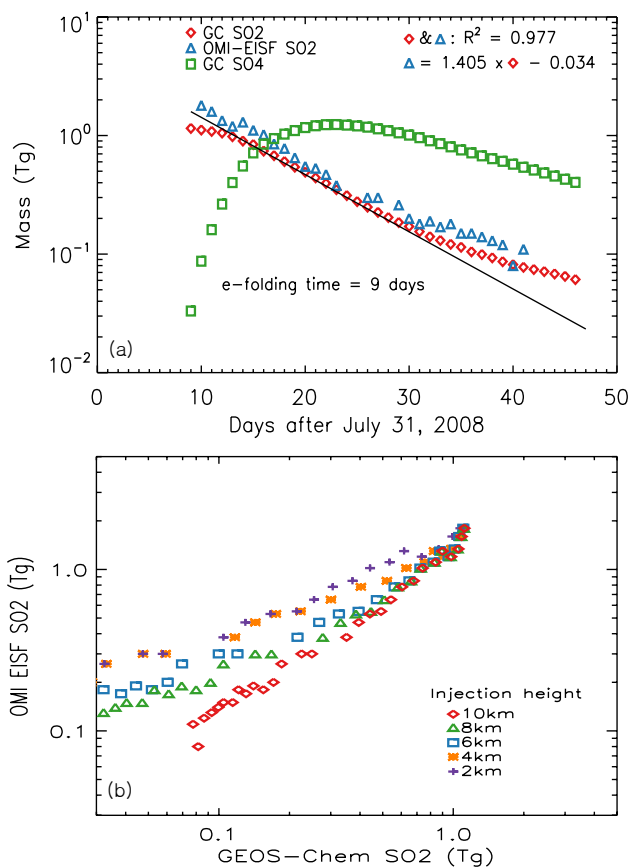
Fig. 3. (a) Time series of daily total volcanic SO_2 mass (in log-scale on y-axis) after the Kasatochi eruption. Red diamonds and blue triangles are the results from the GEOS-Chem simulation and OMI retrievals, respectively. Also overlaid is the GEOS-Chem simulated total volcanic SO_4^{2-} mass (green squares). The solid black line is a linear least-squares-fit between the GEOS-Chem simulated SO_2 mass (log scale) and the number of days after the eruption, from which an e-folding time of 9 days for SO_2 is derived. Also shown at the top right is the equation for a linear least-squares-fit between GEOS-Chem simulated and OMI retrieved SO_2 as well as their linear correlation coefficient (R). **(b)** Scattered diagram of daily total volcanic SO_2 mass between GEOS-Chem (with each injection height) and OMI retrievals. Note, the time series of OMI SO_2 data is obtained from Krotkov et al. (2010), in which the data points in the first two days are estimated based upon the extrapolation to account for OMI's sampling bias due to limited spatial and temporal coverage.

7.5–12 km, and 40 % 12-14 km), their modeled averages of sulfate AOD over the Northern Hemisphere between 0° N and 85° N for Kasatochi eruption peaked in early September centered around 7 September, which is about 9 days earlier than that is derived based upon OSIRIS AOD (at 750 nm) data. Figure 3 in Kravitz et al. (2012) further showed that the peak value (0.006) of zonal averages of OSIRIS AOD first appeared on 1September at 55° N and then expanded to the northern latitude region in the following 30–40 days. It

is noted that the statistics from OSIRIS AOD data can be affected by its limitations in spatial and temporal sampling (because OISIRIS is a limb sensor measuring the visible light). Furthermore, the value of averages of AOD not only depends on the SO_4^{2-} mass, but also is subject to how SO_4^{2-} mass is distributed spatially, the aerosol scattering properties and the relative humidity simulated or prescribed in the model. Hence, instead of using AOD or SO_4^{2-} to quantitatively evaluate the model, we conduct the quantitative comparison with SO_2 data derived from OMI, and further qualitatively evaluate the model with AOD data from MODIS and CALIOP.

Based on the OMI SO_2 data for 14–31 August 2008 (i.e., blue triangles in Fig. 3a), Krotkov et al. (2010) estimated an e-folding time for the Kasatochi SO_2 of around 9 days. Interestingly, an identical e-folding time is obtained in our GEOS-Chem model simulation for the same time period, which suggests that the oxidation rate for converting SO_2 to sulfate (e.g., the first-order sink rate) in the upper troposphere and low-level stratosphere has no systematic bias in the model, and is consistent with that derived from OMI retrievals. However, the persistent underestimate in the modeled SO_2 columns as shown in Figs. 2 and 3a may reflect a larger sink term or overestimation of oxidant abundance during early plume evolution when SO_2 underwent aqueous-phase oxidation in clouds. This hypothesis is evaluated below by comparing the cloud fraction and LWP in the GEOS-5 meteorological fields with those retrieved by MODIS because in-cloud oxidation is a major sink for atmospheric SO_2. Figure 3b also illustrates the comparison of daily total SO_2 mass between GEOS-Chem and OMI-EISF retrievals. As injection height is lowered from 10 through 2 km, the reduction rate of total SO_2 mass drastically increases with associated e-folding time decreasing from 9 days to ∼3 days, indicating that the life time of volcanic SO_2 more depends on injection height rather than injected mass.

Figure 4a illustrates a cloud fraction comparison between GEOS-Chem and MODIS for each cloud fraction bin (i.e., 0.1) over the region of SO_2 cloud transport (30–70° N and 100–175° W) during the early period after the eruption (about 7 days). The GEOS-Chem or GEOS-5 meteorology fields have a low bias when compared to MODIS for cloud fractions less than 0.7, and high bias when cloud fractions are over 0.8. In addition, the probability density function (PDF) of cloud fraction shows that GEOS-5 fields have large (low) frequency of small (larger) clouds when compared to MODIS (Fig. 4a). The comparison of LWP, a first-order indicator of water cloud geometric thickness, between GEOS-Chem and MODIS (Fig. 4b) shows a similar pattern to that of cloud fraction, indicating that: (a) GEOS-5 underestimates the LWP for thin water clouds and overestimates the LWP for thick clouds, and (b) GEOS-5 simulates more smaller and thin clouds and fewer large and thick clouds. Consequently, the GEOS daily total liquid water amount over the study region in the first 7 days after the eruption is always (10–20 %) greater than that characterized by MODIS
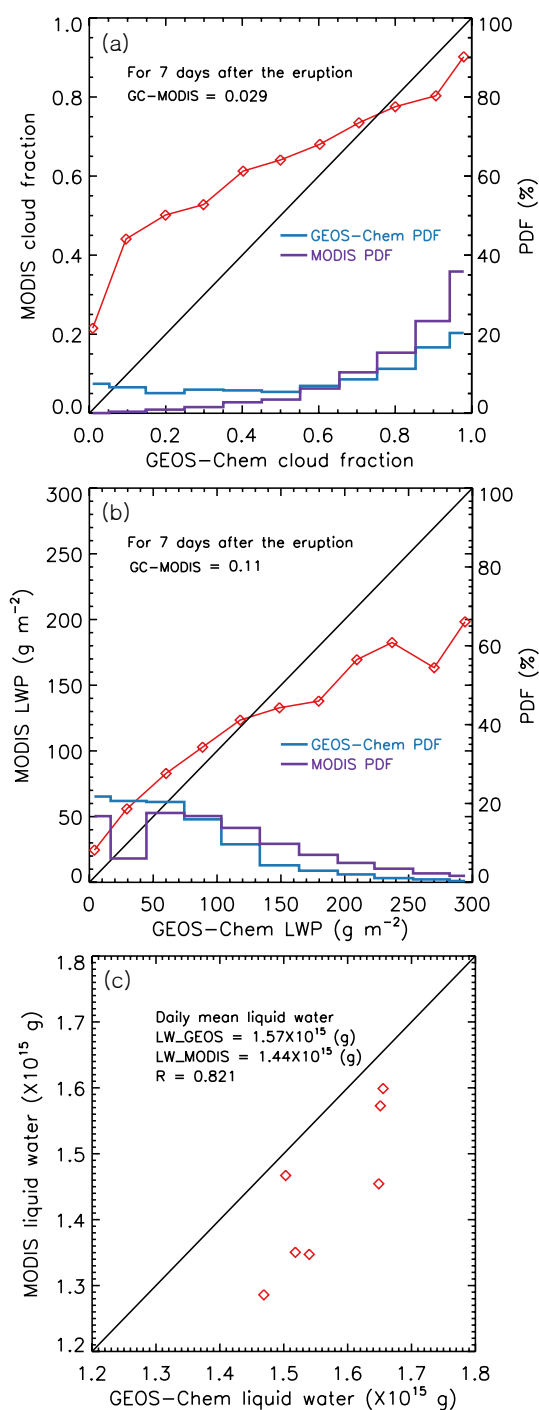
Fig. 4. Comparison (red line) of Cloud fraction **(a)** and LWP (b) derived from GEOS-Chem and MODIS during 7 days after the eruption over the region (30–70° N and 100–175° W). **(c)** comparison of daily total amount of liquid water derived from GEOS-Chem and MODIS for the same time period and region. Also shown in **(a)** and **(b)** are the probability density function (PDF, right y-axis) for each cloud fraction (or LWP) bin from GEOS-Chem (blue line) and MODIS (purple line). In each panel, the linear correlation coefficient (R) and the average difference between GEOS-Chem (GC) and MODIS are also provided.

(Fig. 4c), reflecting the relatively more important contribution of (b), i.e., the overestimation of the number of thin and small clouds in GEOS-5. Presumably, it is those small and thin clouds that can more effectively interact with SO_2 (because of their large area-to-volume ratio). Therefore, during the early period after the eruption, GEOS-Chem overestimates the abundance of liquid water clouds (or oxidants) able to convert volcanic SO_2 into sulfate aerosols in the simulation, which partially explains the model underestimation of SO_2 as shown in Fig. 3. This is especially likely after further consideration that MODIS liquid water path may also has a positive bias (that is ∼10 % in global averages over ocean when compared to the AMSR measurements) (Seethala and Horváth, 2010). Indeed, our sensitivity experiment shows that a reduction of liquid water path by 15 % in the first two days in GEOS-5 field results in a 5 % increase in SO_2 total amount (7 % and 3 % in 1st and 2nd day respectively). It is noted that once SO_2 reaches the upper troposphere and stratosphere, its main sink is oxidation by OH, and hence the consistency of e-folding time between GEOS-Chem simulations and OMI observations (Fig. 3) indicates that oxidation of SO_2 by OH is well represented in the model.

For further evaluation of the model, the simulated distribution of volcanic sulfate AOD is compared with Terra and Aqua MODIS level-2 aerosol data on several selected days when the pathway of volcanic sulfate AOD is easily discernable (Fig. 5). On August 14 (8 days after the eruption), MODIS AOD maps indicate that the volcanic sulfate aerosols (with mid-visible AOD > 0.5) was mainly located over Alaska, Northern Canada, and Northern Mexico (marked respectively as regions A and B in Fig. 5b); such distributions are reasonably reproduced by the GEOS-Chem model simulation in Fig. 5a. The signature of volcanic sulfate aerosols, two weeks after the volcanic eruption, can be further identified over the continental US, Western Atlantic Ocean, and Europe (respectively marked as C-E in both Fig. 5c and d). A period of about 10 days is enough to transport the volcanic aerosols not only over the entire Atlantic Ocean, but also over Asia. About 17 days after the eruption, the volcanic sulfate aerosols are transported zonally from Europe to Eastern Asia (e.g., region G, H, and I in Fig. 5e) and even meridionally to the Southern Pacific Ocean (region F in Fig. 5e). Overall, Fig. 5 shows that the hemispheric distributions of the volcanic sulfate AOD from the simulation are comparable with the MODIS AOD observations.

In addition to using satellite data for evaluating model-simulated column amounts (such as total SO_2 burden and AOD), we also use the CALIOP lidar data to evaluate the vertical profile of aerosol extinction coefficients simulated by the model (Fig. 6). Two CALIPSO orbits (i.e., the solid blue lines in Fig. 5a and e) over North America (region B in Fig. 5a) and East Asia (region I in Fig. 5e) are used for comparison with model simulations. On 14 August 2008, CALIOP data indicate a layer (marked as L1 and L2 in Fig. 6a) with high loading of particles above the tropopause
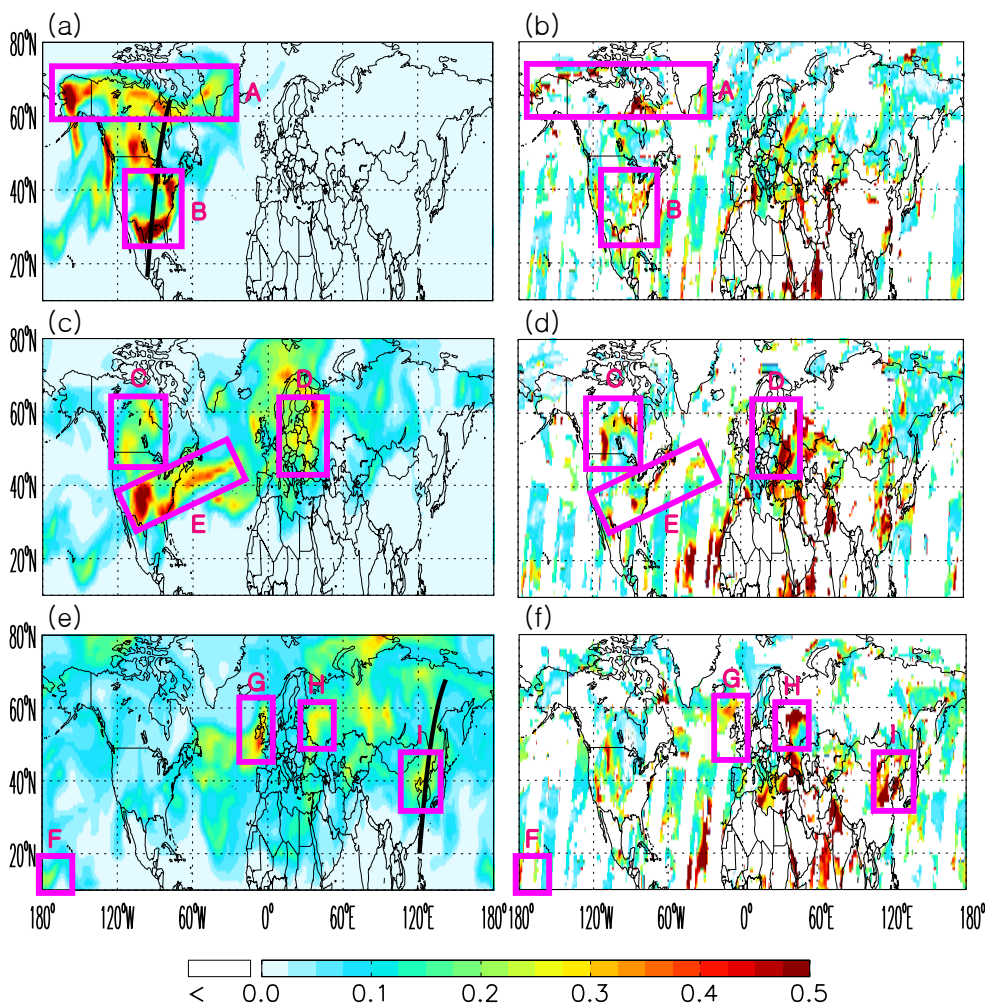
Fig. 5. Spatial distribution of volcanic sulfate aerosol optical depth (AOD) at 550 nm as simulated by GEOS-Chem (left column) and as retrieved by MODIS (right column) on 14 (top row), 19 (middle row), and 25 (bottom row) August 2008, respectively. The solid black lines in **(a)** and **(e)** respectively indicate the ground tracks of CALIOP data that are shown in Fig. 6a and c. The pink rectangles and letters highlight the regions of large volcanic AOD, as discussed in Sect. 4.1.

(black line in Fig. 6b) over North America. Within this layer, the CALIOP measurements of depolarization ratio at 530 nm and backscattering attenuation at 1062 nm both show nearly zero values, and CALIOP layer classification algorithm indicate that this layer are dominated by aerosols with small fraction of cirrus (figures now shown). The model simulation is able to capture a similar vertical distribution of the volcanic sulfate aerosol extinction (marked as L1 and L2 in Fig. 6b), although the coarser model resolution in the stratosphere cannot resolve the very thin-layer structure of the sulfate aerosols detected by CALIOP data. The stratospheric sulfate aerosols are also distinctly detected by CALIPSO on the ∼17th day after the eruption over East Asia (marked as L5, L6, and L8 in Fig. 6c), and those are plausibly captured by the GEOS-Chem simulation in Fig. 6d, especially the descending path of aerosols from Siberia, to East Asia, and to

the western North Pacific (marked respectively as L5, L6, and L8 in both Fig. 6c and d). In addition, CALIOP images in Fig. 6a and b also indicate the likely deposition of volcanic sulfate aerosols in the middle-to-lower atmosphere such as over the south central US (marked as L3 and L4 in Fig. 6a and b) and over northeast China (marked as G in Fig. 6c and d); these "touch down" features are also seen in the similar curtain plots showing the difference in GEOS-Chem simulation with and without considering volcanic aerosols, although non-volcanic aerosols from local source also contribute to the high loading of particles in regions L3 and L7 (figures now shown here).

Quantitatively, the temporal evolution of daily and zonally averaged mean sulfate AOD from the model and the CALIPSO level 2 aerosol products are illustrated in Fig. 7. GEOS-Chem simulations show large amounts of volcanic
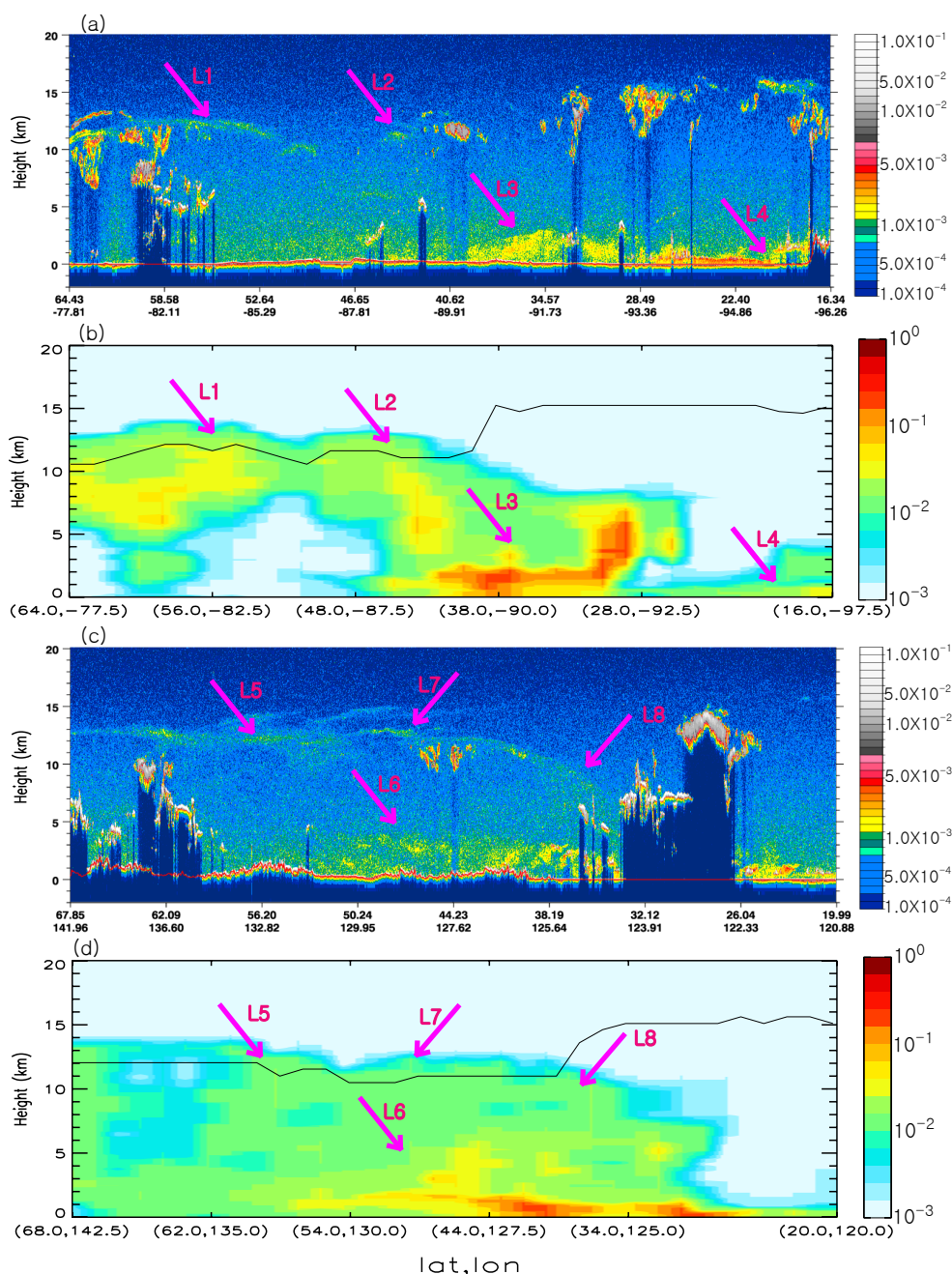
Fig. 6. (a) vertical distribution of 532 nm total attenuated backscatter (km^{-1} sr^{-1}) measured by the CALIOP lidar, and **(b)** the corresponding distribution of tropopause (black line) and the simulated sulfate aerosol extinction coefficient (km^{-1}) at 550 nm for the CALIPSO ground track in Fig. 5a on 14 August 2008. **(c)** and **(d)** are respectively the same as **(a)** and **(b)** for the CALIPSO ground track solid black line in Fig. 5e. The pink arrows and letters highlight the regions of large volcanic AOD, as discussed in Sect. 4.1.

sulfate aerosol in the entire atmosphere (Fig. 7a) with a significant fraction of the aerosol in the stratosphere (Fig. 7b). The GEOS-Chem simulated sulfate AOD is compared with AOD from CALIPSO in Fig. 7c and d only for altitudes over 10 km to minimize the influence of non-volcanic sulfate aerosols in the CALIOP data. It is apparent that the model produces a comparable AOD (mean AOD is ∼0.06)

to that observed by CALIOP from 60–80° N. During the first 30 days after the eruption; the modeled and observed stratospheric AODs are very comparable. The modeled AOD, however, is drastically decreased, while the satellite measured AOD is only slightly decreased after the first 30 days. Some discrepancy may be explained by the misclassification of high cirrus cloud as aerosol in the CALIOP
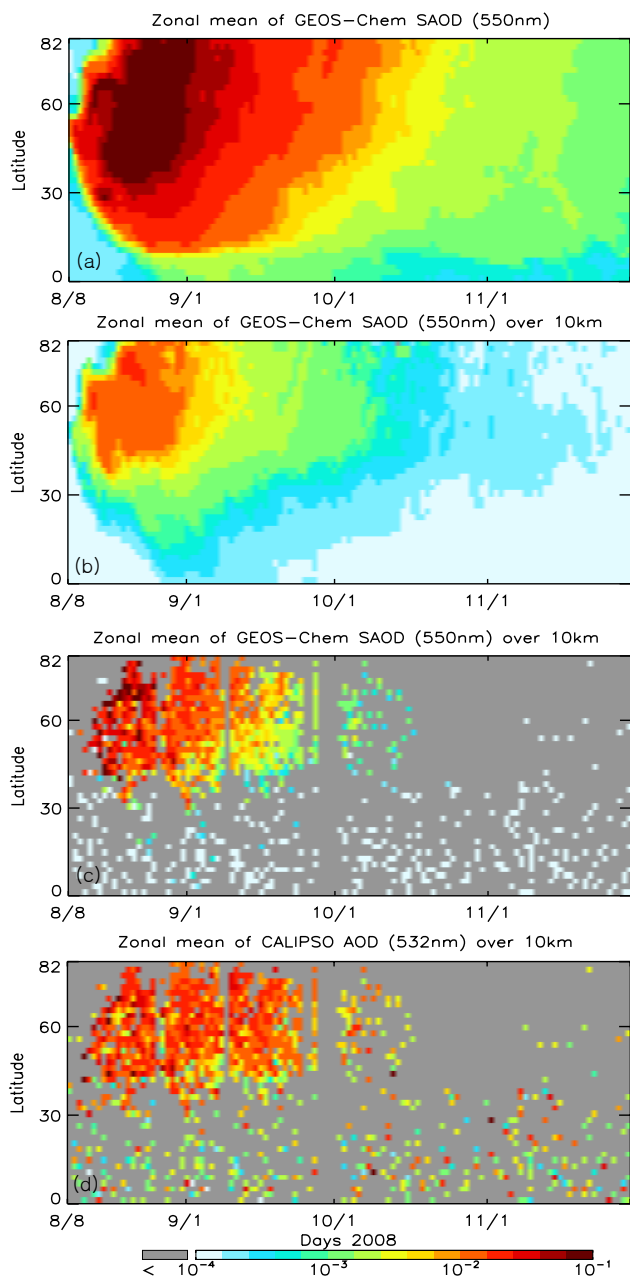
Fig. 7. (a) Temporal evolution of zonally averaged volcanic sulfate aerosol optical depth (SAOD) from GEOS-Chem simulations, **(b)** same as **(a)** but for SAOD above 10 km from the surface, **(c)** the same as **(b)** but SAOD sampled along the CALIOP ground track, and **(d)** same as **(c)** but based upon the analysis of CALIOP level-2 aerosol layer product with the consideration of data quality flags.

algorithm; indeed, the temporal evolution of the zonally averaged backscattering ratio from CALIOP as shown in Vernier et al. (2011) is more similar to the GEOS-Chem simulation in Fig. 7b. In addition, as discussed in Heard et al. (2012), volcanic sources other than Kasatochi, such as the ongoing eruption from Kilauea volcano (19.4° N, 155.3° W) in 2008

may also contribute to the slower decrease of AOD above 10 km in the CALIOP data. About 70 days after the eruption, stratospheric aerosol is no longer detected in satellite data over middle and high latitudes, and the simulated sulfate AOD is also very small ($\sim 4 \times 10^{-4}$). About 100 days after the eruption, the stratospheric sulfate AOD in the model is negligible with daily values of 10^{-4}.

4.2 Baseline results for volcanic sulfate forcing

Figure 8 shows the monthly averaged direct shortwave (SW) radiative forcing by the volcanic sulfate aerosols at the top of the atmosphere (TOA) after the Kasatochi eruption. In monthly and global averages, the clear sky and all sky shortwave forcing of volcanic sulfate aerosols are both strongest (i.e., most negative) in the first month after the eruption, with respective values of $-2.0\,\mathrm{W\,m^{-2}}$ and $-1.3\,\mathrm{W\,m^{-2}}$ (Fig. 8a–b); they steadily become weaker with respective values of -1.0 and $-0.7\,\mathrm{W\,m^{-2}}$ in the second month (Fig. 8e–f), and -0.04 and -0.03 in the 6th month (Fig. 8i–j). Geographically, the volcanic sulfate aerosols are not transported to the Southern Hemisphere until the 2nd month after the eruption, and do not spread over the whole Southern Hemisphere until 30 September 2008. Indeed, most of the volcanic sulfate aerosols remained north of 20° N in the first month after the eruption (Fig. 8a). The difference in radiative forcing between clear and all sky depends, to a large extent, on the cloud fraction and relative altitude of the sulfate aerosol layer and clouds. Since sulfate particles and cloud droplets are highly scattering at visible wavelengths where the solar spectrum peaks, cloud layers, whether underlying or overlying the aerosol layer, generally reduce the spectral contrast between the bright aerosol layer and darker land/ocean surface when viewed from the TOA. As such, cloud layers often reduce the clear-sky radiative forcing of scattering aerosols (Wang et al., 2008). Hence, comparing the third and fourth columns in Fig. 8c, g and k show that the difference between clear-sky and all-sky radiative forcing is small (large) in regions where cloud fraction is low (high) such as over the Saharan desert and the dry regions of the central-to-east Pacific (cloudy regions include the southern ocean at 40–60° S, the tropics, and high latitudes). As expected, over Greenland where surface albedo is high (radiatively acting like a cloud layer), the clear and cloudy sky forcing is nearly the same.

A daily time series of global averages of sulfate aerosol all-sky radiative forcing at the TOA is shown in Fig. 9. Soon after the Kasatochi eruption, the continuous conversion of SO_2 into sulfate results in a steady increase of sulfate AOD and a correspondingly stronger SW radiative forcing at the TOA. The forcing reaches its peak ($-2.1\,\mathrm{W\,m^{-2}}$) about 16 days after the eruption, and thereafter decays exponentially with time (Fig. 9). In contrast, Earth Radiation Budget Experiment data shows that the peak forcing (global average) of sulfate aerosols from Pinatubo eruption (15° N, 121° E) on 15 June 1991 is at least $-4\,\mathrm{W\,m^{-2}}$ in September–October
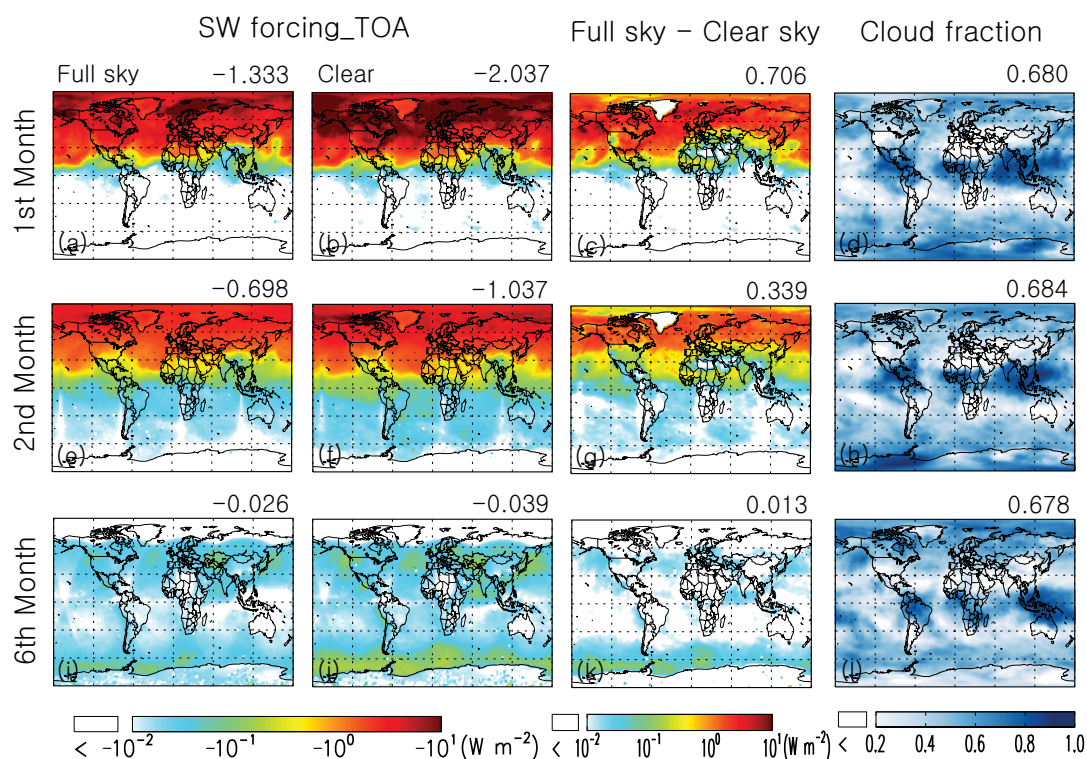
Fig. 8. Averages of volcanic sulfate shortwave (SW) radiative forcing (Wm^{-2}) at the top of the atmosphere (TOA) for all sky **(a)** and clear sky **(b)** conditions, as well as their differences **(c)** in the first month **(a–c)**, second month **(e–g)**, and the 6th month **(i–k)** after the Kasatochi eruption on 8 August 2008. Also shown are the corresponding distributions of cloud fraction **(d, h** and **l)**. Denoted on the top right of each panel is the global average (weighted by gridbox area) of the corresponding quantity.
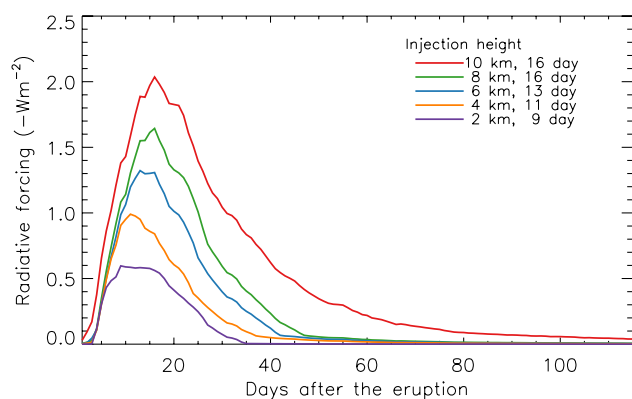

Fig. 9. Temporal evolutions of the daily, global mean volcanic sulfate radiative forcing (Wm^{-2}) at the top of the atmosphere (TOA) for 5 different volcanic SO$_2$ injection heights ranging from 10 km (shown in red line) to 2 km (shown in purple) with interval of 2 km (see legend on the top right for details). Also shown in the legend, corresponding to each injection height used in the GEOS-Chem simulation, are days (after the eruption on 8 August 2008) when the peak of the shortwave forcing occurs.

1991 (Minnis et al., 1993). The significant larger effect of Pinatubo eruption on climate is in part due to the following factors: (a) it ejected ∼30 Tg of SO$_2$ up to 30 km above the sea level, most of which concentrated in 20–27 km altitude (McCormick et al., 1995); (b) at this altitude range over the subtropics, the intensity of planetary wave activity and the phase of the quasi-biennial oscillation regulates the poleward transport, but were shown to be not effective in the Northern Hemisphere in June–July 1992; (c) the spread of SO$_2$ to the subtropics in Southern Hemisphere is found to be unexpectedly faster in June–July 1991, which is attributed to the abnormality of the planetary wave activates over the equator and southern subtropics (Trepte et al., 1993); (d) consequently, SO$_2$ amount was mainly located in the 30° N–30° S in the first several months after Kasatochi eruption, and the larger and longer solar illumination in tropic and subtropics enhance the shortwave forcing of volcanic sulfate particles. In comparison, while the volcanic sulfate aerosols from the Kasatochi eruption (52.1° N, 175.5° W) can reach the tropics within 1–2 month, most of them are concentrated in the mid- and high-latitudes (due to the westerly waves) during Northern Hemisphere fall-winter season (Fig. 8), and their amount (1–2 Tg) and e-folding time (9 days) are both much less than counterparts (30 Tg and ∼1 yr) of Pinatubo eruption

(McCormick et al., 1995). Consequently, Kasatochi eruption may have only affected the global radiative energy budget for about 100 days, and has much less impact on climate.

The timeline of our simulated volcanic sulfate forcing is consistent with model experiment's by Kravitz et al. (2012) that showed all volcanic sulfate aerosols might have been deposited out of the atmosphere by February 2009, and the noticeable forcing may deceased even quicker. A direct quantitative comparison with the results from Kravitz et al. (2012) is complicated by: (a) the model difference in spatial resolution and temporal resolution ($4° \times 5°$ and focus of monthly scale in their climate model), chemical mechanisms (only prescribed OH field available in their model to oxidize SO_2 in the stratosphere), and cloud fields (simulated solely with a climate model), and (b) the definition of sulfate forcing in which aerosol forcing feedback on stratospheric thermal adjustment are considered in their model. Nevertheless, because of sulfate particle is highly scattering (with the single scattering albedo value close to 1) in visible and other shortwave spectrum, our estimate of global forcing at the TOA and surface is very similar, with a global averages of $-1.3\,\mathrm{Wm^{-2}}$ in August and $-0.7\,\mathrm{Wm^{-2}}$ forcing in September, which appear consistent with results in Kravitz et al. (2012) showing a $-2\,\mathrm{Wm^{-2}}$ of zonal averages of forcing at the surface over the Northern Hemisphere in August and September.

4.3 Sensitivity experiment to SO_2 injection height

In order to investigate the effect of volcanic SO_2 plume injection height on SW radiative forcing, we conducted sensitivity simulations with injection heights of 2, 4, 6 and 8 km. Figure 9 shows that the radiative forcing has a strong dependence on the volcanic SO_2 injection height. As the injection height decreases, the magnitude and the duration of the forcing decreases. For example, for a 2 km injection height, the peak forcing is $-0.6\,\mathrm{W\,m^{-2}}$ and the sulfate aerosols influence SW radiation for about 35 days, which contrasts with $-2.1\,\mathrm{W\,m^{-2}}$ and about 100 days when injection height is set at 10 km.

Since the temporal evolution of the volcanic sulfate SW radiative forcing shown in Fig. 9 appears to follow a lognormal distribution, the following function is found to provide a good fit to the forcing-time curves in Fig. 9 for different injection heights:

$$y = \frac{S_1 e^{-2(\ln x S_2)^2}}{x S_2 \sqrt{\frac{\pi}{2}}},$$

where $x =$ injection height (km), $y =$ parameterized radiative forcing ($\mathrm{W\,m^{-2}}$), and the two scale factors are a function of injection height x: $S_1 = 0.4x + 0.5$, and $S_2 = -0.00375x + 0.0875$. It is found that the parameterized SW radiative forcing agrees with the GEOS-Chem simulated forcing for each injection height as a function of number of days after the eruption, with linear correlation coeffi-

cients generally larger than 0.98 (Fig. not shown). As shown in Fig. 10, the parameterization adequately reproduces the peak value of the radiative forcing (Fig. 10b) and the timing for this peak value (Fig. 10a) for different injection heights. Based upon this parameterization, a difference of 2 km in injection height can lead to a 0.4 % difference in the overall estimate of the forcing effect (e.g., forcing multiplied by time) in the whole globe.

4.4 Sensitivity experiment to aerosol size distribution

In our baseline simulation, the sulfate particles are assumed to have a lognormal size distribution with a geometric radius of 0.07 µm and standard deviation of 1.8 µm. In order to investigate the impact of volcanic sulfate particle size on SW radiative forcing at the TOA, sensitivity experiments were conducted to compute the forcing with different sets of sulfate optical properties corresponding to increasing geometric radii from 0.07 µm to 0.19 µm with a step size of 0.03 µm. Wang et al. (2008) showed that as the particle size increases, the associated increase in particle extinction cross section outweighs the associated reduction in backscattering, and thus results in stronger aerosol forcing. As shown in Fig. 11, an increment of 0.03 µm in sulfate particle radius results in an enhancement of $\sim$0.1-0.2 W m^{-2} in the 30-day (after eruption) and global average sulfate all-sky SW radiative forcing at the TOA.

5 Summary and discussion

GEOS-Chem, a global chemical transport model, has been used in conjunction with constraints from the OMI-EISF retrievals of SO_2 amount and effective height to simulate the life cycle of SO_2 and volcanic sulfate aerosols after the 2008 Kasatochi eruption and to study the resultant impact on direct shortwave radiative forcing. With the use of the OMI EISF-based SO_2 product to initialize the SO_2 distribution in GEOS-Chem, the simulated lifetime (with an estimated e-folding time of 9 days) as well as the spatial distribution and temporal evolution of the volcanic SO_2 burden in the atmosphere after the eruption are both in good agreement with OMI SO_2 observations, suggesting that the oxidation of SO_2 in the stratosphere (primarily by the hydroxyl radical, OH) is reliably represented in GEOS-Chem. However, a consistent low ($\sim$25 %) bias is found in the GEOS-Chem simulated SO_2 burden, and comparison with MODIS cloud products indicates that this is likely due to a high ($\sim$20 %) bias in cloud liquid water amount and a resultant stronger oxidation of SO_2 in the GEOS meteorological data during the first week after the eruption when part of SO_2 is oxidized by clouds. Further evaluation with aerosol products from MODIS and CALIOP reveal that GEOS-Chem simulations capture the 3-D transport pathway of volcanic sulfate aerosols including: (a) their longitudinal transport from Alaska to central Canada, and
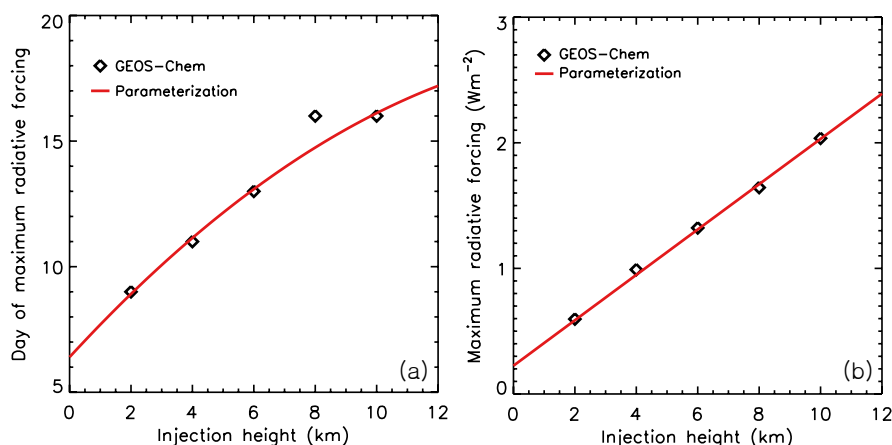
Fig. 10. (a) Scatter plot of the volcanic SO_2 injection height (km) and the days (after the eruption) when the peak of daily and global averages of volcanic sulfate shortwave forcing occurs. The data are based upon results in Fig. 9. **(b)** same as **(a)** but shows the peak value of the daily and global average of volcanic sulfate shortwave forcing. The red lines in **(a)** and **(b)** respectively show the results based upon the parameterizations as described in Sect. 4.3.
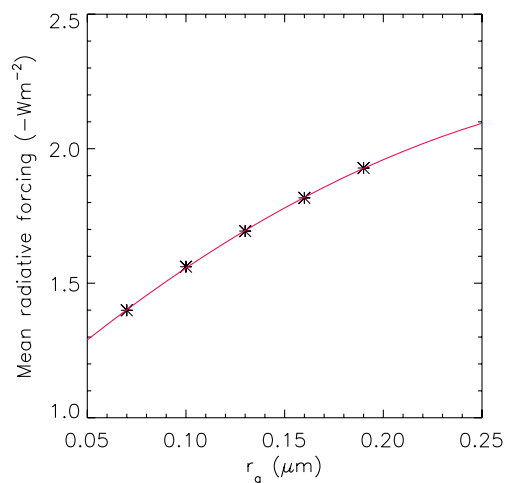

Fig. 11. Global and 30-day (after eruption) average of volcanic sulfate shortwave forcing at the top of atmosphere as a function of the geometric radius (r_g) used in the log-normal size distribution to describe the aerosol optical properties in the forcing calculation.

then to the south central Great Plains in the first two weeks, as well as (b) their zonal transport from high-latitude regions of North America to mid- and high-latitude regions in Europe and Asia, and the consequent transport from Siberia to southeast China within three weeks after the eruption.

Radiative transfer calculations show that the all-sky direct radiative forcing at the TOA due to the Kasatochi volcanic sulfate aerosols reached a peak in the late second week and early third week post-eruption, with a daily, global average value of $\sim 2\,W\,m^{-2}$. Consequently, in global and monthly averages, the volcanic sulfate forcing from the Kasatochi eruption peaks up to $-1.3\,W\,m^{-2}$ in the first month after the eruption, with majority of the forcing-influenced region lo-

cated north of $20°\,N$; and then gradually weakens to less than $-0.1\,W\,m^{-2}$ four months after the eruption. The volcanic aerosol forcing doesn't influence the entire Northern Hemisphere until the middle of the second month after the eruption. It is found that clouds can effectively reduce the magnitude of the volcanic sulfate forcing by 20–40 %, on average.

Sensitivity analysis shows that accurate description of the SO_2 injection height and the initial 3-D distribution of SO_2 in the CTM are both critical for reliable simulation of the lifetime and spatiotemporal distribution of volcanic SO_2 and aerosols after the eruption. For the Kasatochi eruption, it is shown that the temporal evolution of the volcanic sulfate forcing can be parameterized using a log-normal distribution as a function of injection height and number of days after the eruption. This parameterization indicates that every 2 km reduction of SO_2 injection height results in a 2 day decrease in SO_2 lifetime and $0.4\,W\,m^{-2}$ reduction in forcing (in global and daily averages). Further sensitivity tests also showed that every 0.03 µm increase of geometric particle radius used in the log-normal size distribution for describing aerosol optical properties leads to ~ 25 % increase in the magnitude of the forcing, although the rate of increase falls off for larger geometric radii.

This study is among the first to assimilate both satellite-based SO_2 plume height and column amount into a CTM for an improved simulation of volcanic SO_2 transport, which has important implications for studies of natural climate forcing as well as for forecasts of atmospheric opacity that impacts aviation safety.

References

Ackerman, S. A., Strabala, K. I., Menzel, W. P., Frey, R. A., Moeller, C. C., and Gumley, L. E.: Discriminating clear sky from clouds with MODIS, J. Geophys. Res., 103, 32141–32157, 1998.

Alexander, B., Park, R. J., Jacob, D. J., and Gong, S.: Transition metal-catalyzed oxidation of atmospheric sulfur: global implications for the sulfur budget, J. Geophys. Res., 114, D02309, doi:10.1029/2008JD010486, 2009.

Andres, R. J. and Kasgnoc, A. D.: A time-averaged inventory of subaerial volcanic sulfur emissions, J. Geophys. Res., 103, 25251–25261, 1998.

Barnes, S. L.: A technique for maximizing details in numerical weather map analysis, J. Appl. Meteor., 3, 396–409, 1964.

Bey, I., Jacob, D. J., Yantosca, R. M., Logan, J. A., Field, B., Fiore, A. M., Li, Q., Liu, H., Mickley, L. J., and Schultz, M.: Global modeling of tropospheric chemistry with assimilated meteorology: Model description and evalustion, J. Geophys. Res., 106, 23073–23096, 2001.

Bond, T. C., Bhardwaj, E., Dong, R., Jogani, R., Jung, S., Roden, C., Streets, D. G., and Trautmann, N. M.: Historical emissions of black and organic carbon aerosol from energy-related combustion, 1850–2000, Global Biogeochem. Cy., 21, GB2018, doi:10.1029/2006GB002840, 2007.

Budyko, M. I.: Climatic Changes, AGU, Washington, DC, USA, 261 pp., doi:10.1029/SP010, 1977.

Burrows, J. P., Weber, M., Buchwitz, M., Rozanov, V., Ladstätter-Weißenmayer, A., Richter, A., DeBeek, R., Hoogen, R., Bramstedt, K., Eichmann, K.-U., Eisinger, M. and Perner, D.: The Global Ozone Monitoring Experiment (GOME): Mission concept and first scientific results, J. Atmos. Sci., 56, 151–175, 1999.

Carn, S. A., Krueger, A. J., Bluth, G. J. S., Schaefer, S. J., Krotkov, N. A., Watson, I. M., and Datta, S.: Volcanic eruption detection by the Total Ozone Mapping Spectrometer (TOMS) instruments: A 22-year record of sulphur dioxide and ash emissions, in Volcanic Degassing, edited by: Oppenheimer, C., Pyle, D. M., and Barclay, J., Spec. Publ. Geol. Soc. Ldn, 213, 177–202, 2003.

Chin, M., Jacob, D. J., Gardner, G. M., Foreman-Fowler, M. S., and Spiro, P. A.: A global three-dimensional model of tropospheric sulfate, J. Geophys. Res., 101, 18667–18690, 1996.

Clarisse, L., Coheur, P. F., Prata, A. J., Hurtmans, D., Razavi, A., Phulpin, T., Hadji-Lazaro, J., and Clerbaux, C.: Tracking and quantifying volcanic SO2 with IASI, the September 2007 eruption at Jebel at Tair, Atmos. Chem. Phys., 8, 7723–7734, doi:10.5194/acp-8-7723-2008, 2008.

Deshler, T., Anderson-Sprecher, R., Jager, H., Barnes, J., Hofmann, D. J., Clemesha, B., Simonich, D., Osborn, M., Grainger R. G., and Godin-Beekmann, S.: Trends in the non-volcanic component of stratospheric aerosol over the period 1971–2004, J. Geophys. Res., 111, D01201, doi:10.1029/2005JD006089, 2006.

Eckhardt, S., Prata, A. J., Seibert, P., Stebel, K., and Stohl, A.: Estimation of the vertical profile of sulfur dioxide injection into the atmosphere by a volcanic eruption using satellite column measurements and inverse transport modeling, Atmos. Chem. Phys., 8, 3881–3897, doi:10.5194/acp-8-3881-2008, 2008.

Evans, M. J. and Jacob, D. J.: Impact of new laboratory studies of N2O5 hydrolysis on global model budgets of tropospheric nitrogen oxides, ozone, and OH, Geophys. Res. Lett., 32, L09813, doi:10.1029/2005GL022469, 2005.

Fisher, J. A., Jacob, D. J., Wang, Q., Bahreini, R., Carouge, C. C., Cubison, M. J., Dibb, J. E., Diehl, T., Jimenez, J. L., Leibensperger, E. M., Lu, Z., Meinders, M. B. J., Pye, H. O. T., Quinn, P. K., Sharma, S., Streets, D. G., van Donkelaar, A., and Yantosca, R. M.: Sources, distribution, and acidity of sulfate-ammonium aerosol in the Arctic in winter-spring, Atmos. Environ., 45, 7301–7318, 2011.

Fairlie, T. D., Jacob, D. J., Dibb, J. E., Alexander, B., Avery, M. A., van Donkelaar, A., and Zhang, L.: Impact of mineral dust on nitrate, sulfate, and ozone in transpacific Asian pollution plumes, Atmos. Chem. Phys., 10, 3999–4012, doi:10.5194/acp-10-3999-2010, 2010.

Fu, T.-M., Jacob, D. J., Wittrock, F., Burrows, J. P., and Vrekoussis, M.: Global budgets of atmospheric glyoxal and methylglyoxal, and implications for formation of secondary organic aerosols, J. Geophys. Res., 113, D15303, doi:10.1029/2007JD009505, 2008.

Frey, R. A., Ackerman, S. A., Liu, Y., Strabala, K. I., Zhang, H., Key, J. R., and Wang, X.: Cloud detection with MODIS, part I: Improvements in the MODIS cloud mask for collection, 5, J. Atmos. Ocean. Technol., 25, 1057–1072, 2008.

Fu, Q. and Liou, K. N.: Parameterization of the radiative properties of cirrus clouds, J. Atmos. Sci., 50, 2008–2025, doi:10.1175/1520-0469(1993)050<2008:POTRPO>.0.CO;2, 1993.

Hansen, J. E., Wang, W.-C., and Lacis, A. A.: Mount Agung provides a test of a global climatic perturbation, Science, 199, 1065–1068, 1978.

Heard, I. P. C., Manning, A. J., Haywood, J. M., Witham, C., Redington, A., Jones, A., Clarisse, L., and Bourassa, A.: A comparison of atmospheric dispersion model predictions with observations of SO2 and sulphate aerosol from volcanic eruptions, J. Geophys. Res., 117, D00U22, doi:10.1029/2011JD016791, 2012.

Hofmann, D. J. and Solomon, S.: Ozone destruction through heterogeneous chemistry following the eruption of El Chichon, J. Geophys. Res., 94, 5029–5041, doi:10.1029/JD094iD04p05029, 1989.

Intergovernmental Panel on Climate Change (2007), Climate Change 2007: The Physical Science Basis. Contribution of Working Group I to the Fourth Assessment. Report of the Intergovernmental Panel on Climate Change, edited by S. Solomon et al., Cambridge Univ. Press, Cambridge, UK

Karagulian, F., Clarisse, L., Clerbaux, C., Prata, A. J., Hurtmans, D., and Coheur, P. F.: Detection of volcanic SO2, ash, and H2SO4 using the Infrared Atmospheric Sounding Interferometer (IASI), J. Geophys. Res., 115, D00L02, doi:10.1029/2009JD012786, 2010.

King, M. D., Menzel, W. P. Kaufman, Y. J., Tanré, D., Gao, B.-C., Platnick, S., Ackerman, S. A., Remer, L. A., Pincus, R. and Hubanks, P. A.: Cloud and aerosol properties, precipitable water, and profiles of temperature and water vapor from MODIS, IEEE Trans. Geosci. Remote Sens., 41, 442–458, 2003.

Koelemeijer, R. B. A., de Haan, J. F., and Stammes, P.: A database of spectral surface reflectivity in the range 335–772 nm derived from 5.5 years of GOME observations, J. Geophys. Res., 108, 4070, doi:10.1029/2002JD002429, 2003.

Kravitz, B., Robock, A., Bourassa, A., and Stenchikov, G.: Negligible climatic effects from the 2008 Okmok and Kasatochi volcanic eruptions, J. Geophys. Res., 115, D00L05, doi:10.1029/2009JD013525, 2010.

Krotkov, N. A., Schoeberl, M. R., Morris, G. A., Carn, S., and Yang, K.: Dispersion and lifetime of the SO_2 cloud from the August 2008 Kasatochi eruption, J. Geophys. Res., 115, D00L20, doi:10.1029/2010JD013984, 2010.

Krueger, A. J.: Sighting of El Chichon sulfur dioxide clouds with the Nimbus 7 Total Ozone Mapping Spectrometer, Science, 220, 1277–1379, 1983.

Krueger, A. J., Walter, L. S., Bhartia, P. K., Schnetzler, C. C., Krotkov, N. A., Sprod, I., and Bluth, G. J. S.: Volcanic sulfur dioxide measurements from the Total Ozone Mapping Spectrometer (TOMS) instruments, J. Geophys. Res., 100, 14057-14076, 1995.

Kruger, A. J., Schaefer, S., Krotkov, N., Bluth, G., and Barker, S.: Ultraviolet remote sensing of volcanic emissions and applications to aviation hazard mitigation Remote Sensing of Active Volcanism, Geophys. Monogr., 116, 25–43, 2000.

Lee C., Martin, R. V., van Donkelaar, A., Lee, H., Dickerson, R. R., Hains, J. C., Krotkov, N., Richter, A., Vinnikov, K., and Schwab, J. J.: SO_2 emissions and lifetimes: Estimates from inverse modeling using in situ and global, space-based (SCIAMACHY and OMI) observations, J. Geophys. Res., 116, D06304, doi:10.1029/2010JD014758, 2011.

Levelt, P. F., Hilsenrath, E., Leppelmeier, G. W., van den Oord, G. H. J., Bhartia, P. K., Tamminen, J., de Haan, J. F., and Veefkind, J. P.: Science objectives of the Ozone Monitoring Instrument, IEEE Trans. Geosci. Remote Sens., 44, 1199–1208, doi:10.1109/TGRS.2006.872336, 2006.

Liu, H., Jacob, D. J., Bey, I., and Yantosca, R. M.: Constraints from ^{210}Pb and ^7Be on wet deposition and transporting a global three-dimensional chemical tracer model driven by assimilated meteorological fields, J. Geophys. Res., 106, 12109–12128, 2001.

Mari, C., Jacob, D. J., and Bechtold, P.: Transport and scavenging of soluble gases in a deep convective cloud, J. Geophys, Res., 105, 22255–22267, 2000.

McLinden, C. A., Olsen, S. C., Hannegan, B., Wild, O., Prather, M. J., and Sundet, J.: Stratospheric ozone in 3-D models: a simple chemistry and the cross-tropopause flux, J. Geophys. Res., 105, 14653–14665, 2000.

Min, Q., Joseph, E., Lin, Y., Min, L., Yin, B., Daum, P. H., Kleinman, L. I., Wang, J., and Lee, Y.-N.: Comparison of MODIS cloud microphysical properties with in-situ measurements over the Southeast Pacific, Atmos. Chem. Phys., 12, 11261–11273, doi:10.5194/acp-12-11261-2012, 2012.

Minnis, P., Harrison, E. F., Stowe, L. L., Gibson, G. G., Denn, F. M., Doelling, D. R., and Smith Jr., W. L.: Radiative climate forcing by the Mount Pinatubo eruption, Science, 259, 1411–1415, 1993.

Munro, R., Eisinger, M., Anderson, C., Callies, J., Corpaccioli, E., Lang, R., Lefebvre, A., Livschitz, Y., Pérez Albiñana, A.: GOME-2 on MetOp,Proc. The 2006 EUMETSAT Meteorological Satellite Conference, Helsinki, Finland, EUMETSAT, 48 pp., 92-9110-076-5, 2006.

Olivier, J. G. J. and Berdowski, J. J. M.: Global emissions sources and sinks, In: Berdowski, J., Guicherit, R. and B. J. Heij (eds.), The Climate System, 33–78 pp., Lisse, The Netherlands, 2001.

McCormick, M., Thomason, L. W., and Trepte, C. R.: Atmospheric effects of the Mt Pinatubo eruption, Nature, 373, 399–404, 1995.

Pieri, D. and Abrams, M.: ASTER watches the world's volcanoes: a new paradigm for volcanological observations from orbit, J. Volcanol. Geotherm. Res., 135, 13–28, 2010.

Prata, A. J. and Bernardo, C.: Retrieval of volcanic SO_2 column abundance from Atmospheric Infrared Sounder data, J. Geophys. Res., 112, D20204, doi:10.1029/2006JD007955, 2007.

Price, C. and Rind, D.: A simple lightning parameterization for calculating global lightning distributions, J. Geophys. Res., 97, 9919–9933, 1992.

Remer, L. A., Kaufman, Y. J., Tanré, D., Mattoo, S., Chu, D. A., Martins, J. V., Li, R.-R., Ichoku, C., Levy, R. C., Kleidman, R. G., Eck, T. F., Vermote, E., and Holben, B. N.: The MODIS Aerosol Algorithm, Products, and Validation, J. Atmos. Sci., 62, 947–973, 2005.

Rix, M., Valks, P., Hao, N., Loyola, D., Schlager, H., Huntrieser, H., Flemming, J., Koehler, U., Schumann, U., and Inness, A.: Volcanic SO_2, BrO and plume height estimations using GOME-2 satellite measurements during the eruption of Eyjafjallajökull in May 2010, J. Geophys. Res., 117, D00U19, doi:10.1029/2011JD016718, 2012.

Robock, A.: Volcanic Eruptions and Climate, Rev. Geophys., 38, 191–219, doi:10.1029/1998RG000054, 2000.

Russell, J. M., Luo, M. Z., Cicerone, R. J., and Deaver, L. E.: Satellite Confirmation of the Dominance of Chloroflourocarbons in the Global Stratospheric Chlorine Budget, Nature, 379, 526–529, 1996.

Russell, P. B. et al.: Global to microscale evolution of the Pinatubo volcanic aerosol derived from diverse measurements and analyses, J. Geophys. Res., 101, 18745-18763, 1996.

Seethala, C. and Horváth, Á.: Global assessment of AMSR-E and MODIS cloud liquid water path retrievals in warm oceanic clouds, J. Geophys. Res., 115, D13202, doi:10.1029/2009JD012662, 2010.

Seinfeld, J. H. and Pandis, S. N.: Atmospheric Chemistry and Physics: From Air Pollution to Climate Change, 1203pp., John Wiley, Hoboken, NJ, USA, 2006.

Simkin, T. and Siebert, L.: Volcanoes of the World, 2nd edition. Geoscience Press in association with the Smithsonian Institution Global Volcanism Program, 368 pp., Tucson, AZ, USA, 1994.

Solomon, S.: Stratospheric Ozone Depletion: a Review of Concepts and History, Rev. Geophys., 37, 275–316, 1999.

Solomon, S., Daniel, J. S., Neely III, R. R., Vernier, J.-P., Dutton, E. G., and Thomason, L. W.: The Persistently Variable "Background" Stratospheric Aerosol Layer and Global Climate Change, Science, 333, 866–870, 2011.

Spiro, P. A., Jacob, D. J., and Logan, J. A.: Global Inventory of Sulfur Emissions with a $1° \times 1°$ Resolution, J. Geophys. Res., 97, 6023–6036, 1992.

Toon, O. B.: Volcanoes and climate, Atmospheric Effects and Potential Climatic Impact of the 1980 Eruptions of Mount St. Helens, edited by A. Deepak, NASA Conf. Publ., 2240, 15–36, 1982.

Trepet, C. R., Veiga, R. E., and McCormick, M. P.: The poleward dispersal of Mount Pinatubo volcanic aerosol, J. Geophys. Res.,

98, 18563–18573, 1993.

van der Werf, G. R., Morton, D. C., DeFries, R. S., Giglio, L., Randerson, J. T., Collatz, G. J., and Kasibhatla, P. S.: Estimates of fire emissions from an active deforestation region in the southern Amazon based on satellite data and biogeochemical modelling, Biogeosciences, 6, 235–249, doi:10.5194/bg-6-235-2009, 2009.

Vernier, J.-P., Thomason, L. W., Pommereau, J.-P., Bourassa, A., Pelon, J., Garnier, A., Hauchecorne, A., Blanot, L., Trepte, C., Degenstein, D., and Vargas, F.: Major influence of tropical volcanic eruptions on the stratospheric aerosol layer during the last decade, Geophys. Res. Lett., 38, L12807, doi:10.1029/2011GL047563, 2011.

Wang, J., Jacob, D. J., and Martin, S. T.: Sensitivity of sulfate direct climate forcing to the hysteresis of particle phase transitions, J. Geophys. Res., 113, D11207, doi:10.1029/2007JD009368, 2008.

Wang, J., Nair, U., and Christopher, S. A.: GOES-8 aerosol optical thickness assimilation in a mesoscale model: Online integration of aerosol radiative effects, J. Geophys. Res., 109, D23203, doi:10.1029/2004JD004827, 2004.

Watson, I. M., Realmuto, V. J. Rose,, W. I., Prata, A. J., Bluth, G. J. S., Gu, Y., Bader, C. E., and Yu, T.: Thermal infrared remote sensing of volcanic emissions using the moderate resolution imaging spectroradiometer, J. Volcanol. Geotherm. Res., 135, 75–89, 2004.

Wesely, M. L.: Parameterization of surface resistance to gaseous dry deposition in regional-scale numerical models, Atmos. Environ., 23, 1293–1304, 1989.

Wilcox, E. M., Harshvardhan, and Platnick, S.: Estimate of the impact of absorbing aerosol over cloud on the MODIS retrievals of cloud optical thickness and effective radius using two independent retrievals of liquid water path, J. Geophys. Res., 114, D05210, doi:10.1029/2008JD010589, 2009.

Wu, S., Mickley, L. J., Jacob, D. J., Logan, J. A., and Yantosca, R. M.: Why are there large differences between models in global budgets of tropospheric ozone?, J. Geophys. Res., 112, D05302, doi:10.1029/2006JD007801, 2007.

Yang, K., Krotkov, N. A., Krueger, A. J., Carn, S. A., Bhartia, P. K., and Levelt, P. F.: Retrieval of large volcanic SO_2 columns from the Aura Ozone Monitoring Instrument: comparison and limitations, J. Geophys. Res., 112, D24S43, doi:10.1029/2007JD008825, 2007.

Yang, K., Krotkov, N. A., Krueger, A. J., Carn, S. A., Bhartia, P. K., and Levelt, P. F.: Improving retrieval of volcanic sulfur dioxide from backscattered UV satellite observations, Geophys. Res. Lett., 36, L03102, doi:10.1029/2008GL036036, 2009.

Yang, K., Liu, X., Bhartia, P. K., Krotkov, N., Carn, S., Hughes, E., Krueger, A., Spurr, R., and Trahan, S.: Direct retrieval of sulfur dioxide amount and altitude from spacebornehyperspectral UV measurements: Theory and application, J. Geophys. Res., 115, D00L09, doi:10.1029/2010JD013982, 2010.

Yevich, R. and Logan, J. A.: An assessment of biofuel use and burning of agricultural waste in the developing world, Global Biogeochem. Cy., 17, 1095, doi:10.1029/2002GB001952, 2003.